ADVANCED FUNCTIONAL MATERIALS
www.afm-journal.de

Ultrahigh Piezoelectricity in Truss-Based Ferroelectric Ceramics Metamaterials

*Jiahao Shi, Kang Ju, Haoyu Chen, Valérie Orsat, Agus P. Sasmito, Ali Ahmadi, and Abdolhamid Akbarzadeh**

Conventional porous ferroelectric materials sacrifice their piezoelectric constants for improving various figures of merit due to a rapidly decreased dielectric constant. Here, novel truss-based ferroelectric metamaterials that simultaneously offer ultrahigh piezoelectric constants and ultralow dielectric constants, originating from the unique combination of truss loading states and polarization direction, are discovered. The homogenization method alongside an analytical model is proposed to predict and elucidate their extraordinary properties, while a customized ferroceramic additive manufacturing platform is resorted to fabricate them. Unlike porous ferroelectrics, ultrahigh piezoelectric constants at low relative densities ($\rho_r \approx 0.1$) are attained. For example, with appropriate scaling, the experimental values of d_{31}, d_{33}, and d_{42} for a ferroelectric octet truss with $\rho_r = 0.1$, can reach 849, −659, and 836 pC N^{-1}, respectively, which are 3.14, 6, and 2 times higher than the counterpart of bulk $BaTiO_3$ ceramics. Combined with the ultralow dielectric constant, extremely high ferroelectric figures of merit, e.g., piezoelectric voltage constant of 11.098 Vm N^{-1}, piezoelectric energy harvesting figure of merit 9422 $\times 10^{-12}$ m^2 N^{-1}, and pyroelectric voltage sensitivity of 56.7 $\times 10^{-3}$ m^2 C^{-1}, are also observed. The multifunctional ferroelectric metamaterials open new avenues for their applications in self-powered ultrasensitive accelerometers, high-performance noncontact sensors, and wearable input devices.

1. Introduction

By tailoring their periodic or non-periodic underlying microarchitectures, metamaterials, as a category of rationally-designed advanced materials can exhibit distinctive and exotic multifunctional properties (e.g., negative optical refractive index,[1] negative effective density,[2] negative Poisson's ratio (NPR),[3] and shape reconfiguration[4]) that surpass those found in natural or chemically-synthesized substances. Multifunctional ferroelectric materials with inherent coupled structural, piezoelectric, and pyroelectric properties[5] are extensively utilized in actuators,[6] sensors,[7] catalysis,[8] and energy harvesters. Efforts to improve the thermo-electromechanical responses of ferroelectric materials have primarily been focused on the engineering of material composition and underlying structures at the micro and/or nanoscale of bulk materials, involving templated grain growth,[9] optimization of grain size,[10] and domain engineering.[10,11] Nevertheless, the rational design of microarchitecture of cellular ferroelectric metamaterials presents a promising strategy to augment their multiphysical properties and remains an area yet to be well explored.

The *piezoelectric* effect converts mechanical oscillations (du/dt where u is displacement and t is time) into electrical power, while the *pyroelectric* effect transforms temperature fluctuations (dT/dt where T is temperature) into electricity.[5] Although porosity in ferroelectric ceramics is commonly regarded as a defect, the deliberate introduction of porosity can be beneficial for specific applications by significantly reducing the dielectric constant (κ_{33}) and volume-specific heat capacity (c_E).[12]

J. Shi, K. Ju, H. Chen, V. Orsat, A. Akbarzadeh
Department of Bioresource Engineering
McGill University
Montreal, QC H9×3V9, Canada
E-mail: hamid.akbarzadeh@mcgill.ca

The ORCID identification number(s) for the author(s) of this article can be found under https://doi.org/10.1002/adfm.202417618

DOI: 10.1002/adfm.202417618

J. Shi, A. Ahmadi
Department of Mechanical Engineering
École de Technologie Supérieure
Montreal, QC H3C 1K3, Canada

J. Shi, A. Ahmadi
University of Montreal Hospital Research Centre (CRCHUM)
Montreal, QC H2×3E4, Canada

A. P. Sasmito
Department of Mining Engineering
McGill University
Montreal, QC H3A 0G4, Canada

A. Akbarzadeh
Department of Mechanical Engineering
McGill University
Montreal, QC H3A 0C3, Canada

For example, the piezoelectric voltage constant ($g_{33} = d_{33}/\kappa_{33}$) and the pyroelectric voltage sensitivity ($F_v = p_3/(c_E\ \kappa_{33})$), which are key in force and temperature sensors, exhibit higher values in porous ferroelectric materials compared to their fully-dense counterparts.[12a] Herein, d_{33} represents the longitudinal piezoelectric constant and p_3 is the pyroelectric constant. In addition to the relative density, pore topology engineering can significantly enhance ferroelectric properties.[12b–e] Compared to ferroelectric foams with random pore architectures,[12b] those with aligned pores parallel to the polarization direction exhibit slightly smaller figures of merit,[12c–e] whereas those with porosity aligned perpendicular to the polarization direction demonstrate much higher values.[12e] For instance, the experimental g_{33} value of ferroelectric foams with perpendicular porosity is almost 2.1 and 3 times higher than foams with random and parallel porosity, respectively, at 0.4 relative density.[12b–e] However, due to the insufficient polarization and inefficient stress transfer, the improvement of these figures of merit comes at the expense of the reduction of the piezoelectric constant d_{33} compared to the constitutive bulk piezoelectric materials (e.g., ≈30%, 25%, and 80% reduction in the d_{33} value of piezoelectric foams with 0.4 relative density with random, parallel, and perpendicular pores have been reported, respectively.[12b–e]) The trade-off between the decreased d_{33} and the decreased dielectric constant hinders the full potential of porous ferroelectric materials for reinforcing their multifunctionality. Furthermore, traditional fabrication methods such as burnt-out polymer spheres (BURPS),[12b] gel casting,[13] replica templating,[14] and freeze casting[12e,15] restrict the realization of ferroelectric metamaterials with truss, plate, or shell nano/microarchitecture.

The mechanical behavior of intricately designed truss-based metamaterials has been extensively studied, revealing intriguing properties such as ultralightness,[16] ultra-stiffness,[16a,17] structural multistability[18] and extreme resilience.[19] Based on the cell topology, lattice materials can be classified as bending-dominated and stretching-dominated. Their Young's modulus (E) and yield strength (σ_y) follow a power law relationship with a relative density as $E/E_s \propto (\rho/\rho_s)^m$ and $\sigma_y/\sigma_{ys} \propto (\rho/\rho_s)^n$, where the subscript s denotes the corresponding properties of the solid material, and the exponents m and n are determined by lattice microarchitectures.[16a,20] Bending-dominated lattices with $m = 2$ and $n = 1.5$ bear loads through the bending of their struts, leading to uneven stress distribution and low material efficiency. In contrast, the struts of mechanically efficient stretching-dominated lattice predominantly deform via uniaxial compression or tension and exhibit linear scaling relationship with relative density, where $m = 1$ and $n = 1$.[20] Maxwell's stability criterion can be applied to determine the deformation mode of lattice materials by assessing the rigidity of their pin-jointed configurations. Mathematically, this is expressed as $M = b - 3j + 6$, where $M > 0$ indicates a stretching-dominated lattice, and $M < 0$ indicates a bending-dominated lattice.[21] Here, b represents the number of struts, and j represents the number of frictionless joints in the 3D truss-based structure. On the other hand, progress in truss-based ferroelectric metamaterials has mainly remained limited to their diverse anisotropic piezoelectric behavior[22] and actuation modes.[6] Leveraging the advantages of additive manufacturing techniques, various architected ferroelectric materials have been investigated,[23] such as gyroid and diamond skeletons, 2D diagonal lattices, and 3D SC lattices. However, a decrease in relative density is associated with weakened piezoelectricity. Although shell-based ferroelectric metamaterials can mitigate the influence of reduction of relative density on the decrease of direct piezoelectric constants,[24] achieving further enhancement of piezoelectric constants through a decrease of relative density remains elusive. Thus, inspired by the mechanical superiority of stretching-dominated lattice structures, it is encouraging to explore the feasibility of achieving simultaneous elevated piezoelectric and reduced dielectric constants in ferroelectric metamaterials.

In this study, we introduce programmable truss-based ferroelectric metamaterials by adjusting their scaling ratios and relative densities, demonstrating exceptionally high piezoelectric constants and ferroelectric figures of merit. A modified multiphysical asymptotic homogenization method, considering the effects of nonuniform local polarization electric fields, and analytical equations are proposed to elucidate the extraordinary characteristics of these ferroelectric metamaterials. The rationally designed cellular ferroelectrics with intricate truss-based geometric features are 3D printed by a customized digital light processing (DLP) technology to deliver giant ferroelectric properties. The proposed design framework introduces an innovative paradigm for creating highly programmable and ultrasensitive lightweight multifunctional ferroelectrics for applications in self-powered vibration/thermal sensors, touchless control devices, wearable input devices, and precise trajectory recognition systems.

2. Results and Discussion

Taking advantage of its high-resolution printing capability, Digital Light Processing (DLP) is employed for the 3D printing of the green body, which consists of the photosensitive polymer Polyethylene Glycol Diacrylate (PEGDA) 250 of 20 wt. %, photoinitiator diphenyl (2, 4, 6-trimethylbenzoyl) phosphine oxide (TPO) of 0.4 wt. %, and ferroelectric ceramic particles $BaTiO_3$ of 79.6 wt. %, as shown in **Figure 1a**. To reduce the viscosity of the slurry and enhance the fluidity of the printing resin, the ferroelectric ceramic particles undergo surface treatment (Figure S1, Supporting Information). The printed green body is then debinded at 550 °C in a vacuum oven (01200-50, Zhengzhou Zylab Instruments Co., Ltd.) to remove the polymer binder, followed by sintering at a high temperature of 1340 °C in an air atmosphere (M1500-12IT, Zhengzhou Zylab Instruments Co., Ltd.) to densify the ferroelectric ceramic particles, resulting in a 22% volume shrinkage that leads to the reduction of the *as-designed* 6 mm size of the octet truss ferroelectric ceramic to an *as-built* 4.7 mm size. The temperature profiles for heat treatments are presented in Figure S2 (Supporting Information).

Electric polarization is a crucial step for activating the ferroelectric properties of sintered piezoceramics. As depicted in Figure 1b, the electric dipoles within the ceramic are initially oriented in random directions, resulting in a lack of overall ferroelectricity. However, after undergoing a high-voltage polarization, these dipoles align themselves along the electric field distributed within the underlying architecture of the ferroelectric material, leading to the preservation of macroscopic ferroelectric properties even without the presence of an external electric field. When the electric field surpasses 1.5 kV mm^{-1}, the sintered bulk

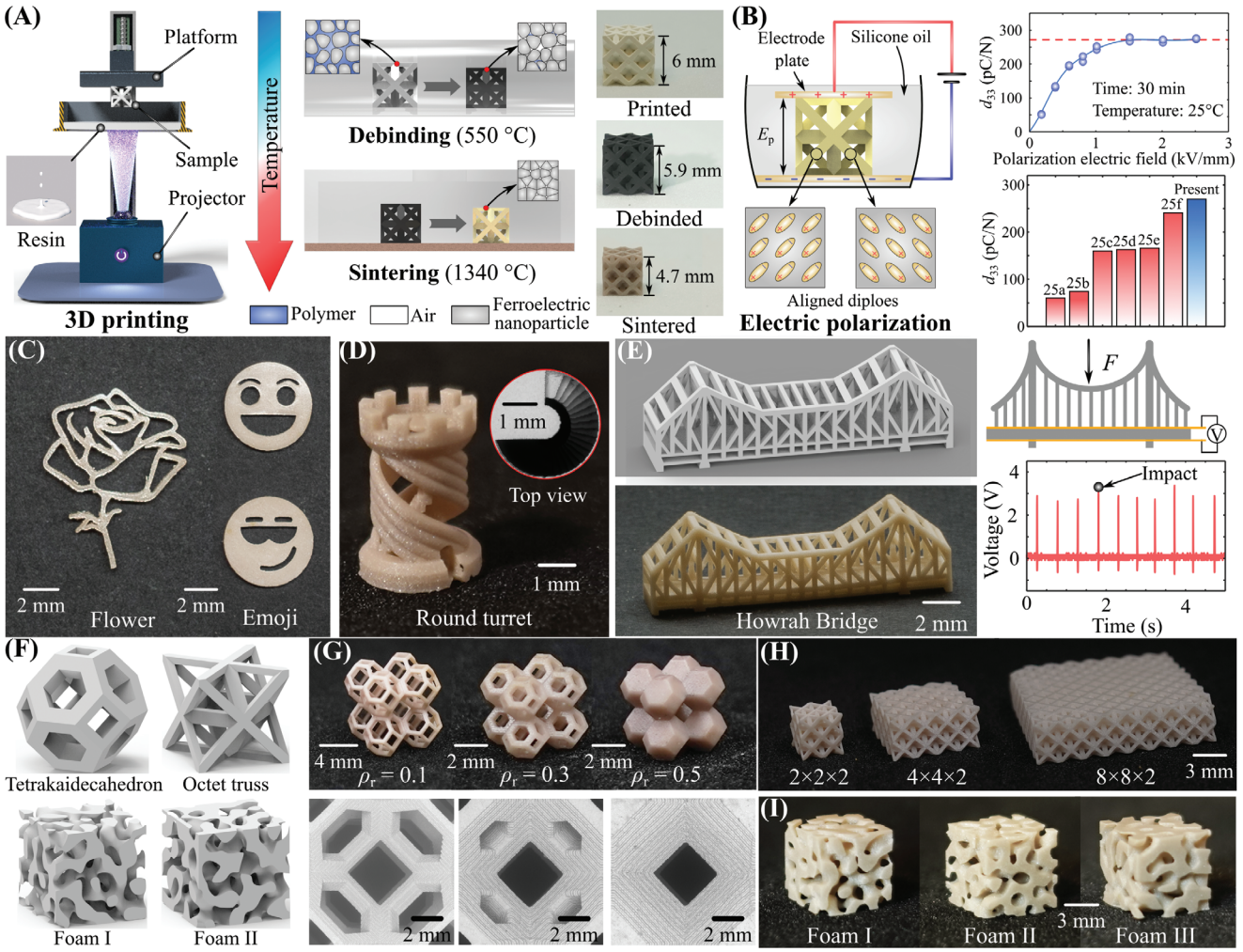

Figure 1. Ferroelectric ceramic 3D printing platform. A) Schematic illustrations of the ferroelectric ceramic fabrication process, including green body DLP printing, debinding, and sintering post-processing. B) Schematics of the electric polarization process of the sintered ferroelectric ceramics and a comparison among the piezoelectric charge constant of the bulk $BaTiO_3$ fabricated in this study and the 3D printed bulk $BaTiO_3$ in the literature. C–E) Optical images of as-fabricated ferroelectric ceramic samples. After polarization, electrodes are attached to the top and bottom surfaces of the Howrah bridge floor, and the voltage response is recorded under an impact load. F) CAD model of the as-designed architected lattices and foams with random architectures. G) Full and enlarged views of fabricated ferroelectric tetrakaidecahedron with different relative densities. Full view of fabricated ferroelectric H) octet truss with alternative numbers of unit cells and I) different types of foams.

$BaTiO_3$ ceramic becomes fully polarized, exhibiting a piezoelectric charge constant d_{33} of 270 pC N^{-1}, as measured by a d_{33} meter (PDK3–2000, PolyK, USA) (Table S1, Supporting Information). This value is higher than that of 3D-printed $BaTiO_3$ ceramics reported in the literature.[25] In this research, our 3D-printed ferroelectric samples are polarized in an oil bath with a 3 kV mm^{-1} electric field for 30 min at room temperature, without encountering electric breakdown. This voltage level is sufficiently high to fully activate the ferroelectric properties.

Our 3D fabrication approach enables the creation of intricate ferroelectric architectures with precise structural features (Figure 1c–f). As an example, a 3D printed and miniaturized intelligent Howrah bridge, constructed out of ferroelectric ceramics, demonstrates a voltage response to external impact loads due to its piezoelectric properties. Inspired by mechanical metamaterials, we utilize the two most representative truss-based structures—stretching-dominated octet truss and bending-dominated tetrakaidecahedron—to construct ferroelectric metamaterials for primary investigation. For comparison with conventional porous ferroelectric ceramics, we employ foam structures that represent the porous ferroelectric ceramics produced by the most widely used BURPS method. Figure 1g,h illustrates the capability of the developed ceramic fabrication platform to 3D print ferroelectric metamaterials with alternative relative densities, numbers of unit cells, and topological structures. Combined with our proposed design strategy, this fabrication technique can serve as a feasible tool for realizing high-performance ferroelectric metamaterials across various microarchitectures.

Commonly, the longitudinal (d_{33}) and transverse ($-d_{31}$) piezoelectric coefficients reduce as the porosity increases for porous ferroelectric ceramics. This decrease in coefficients is attributed to a compromised polarization process efficiency by the increase

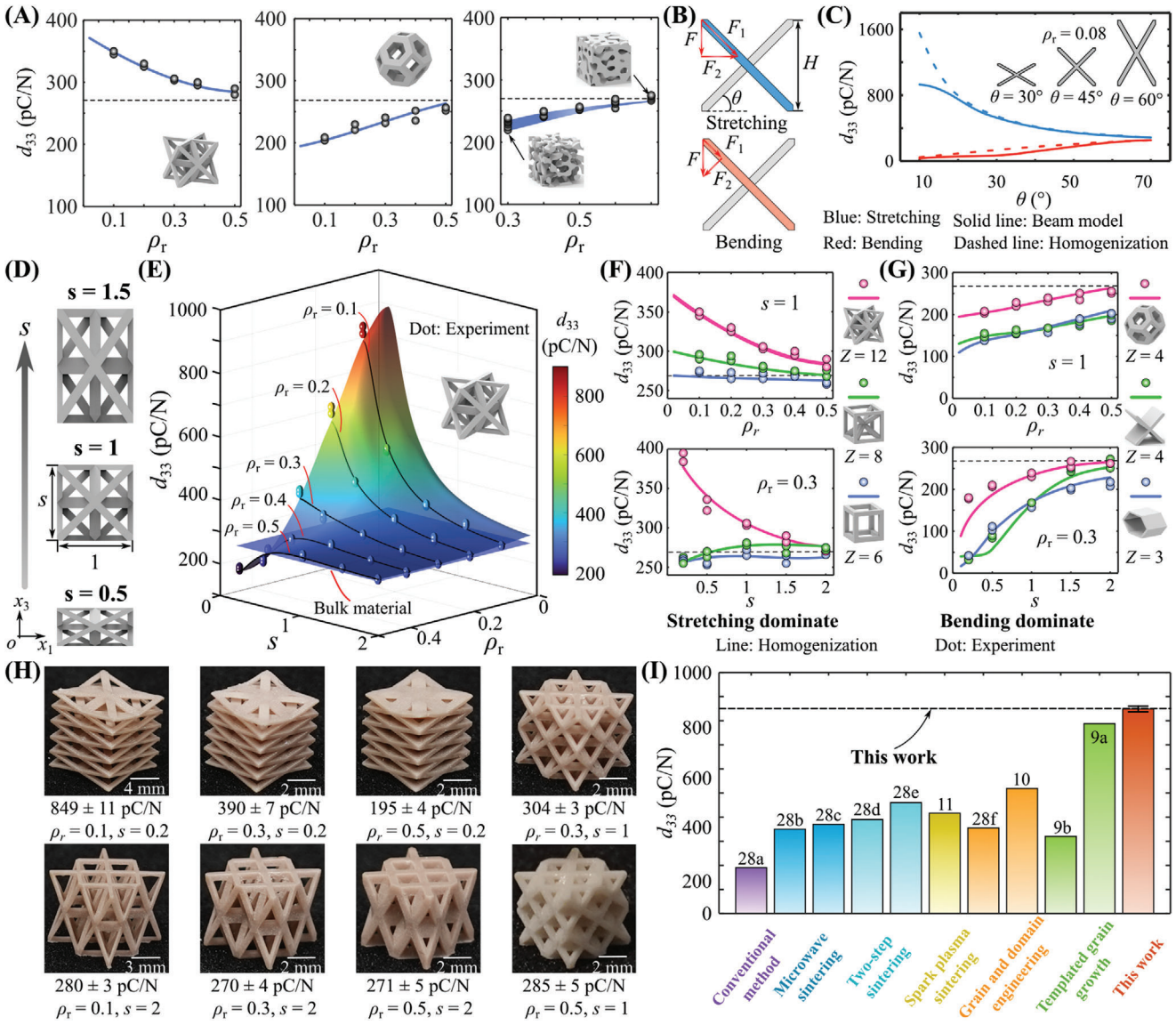

Figure 2. Longitudinal piezoelectric charge constant d_{33} for different ferroelectric lattice metamaterials. A) Examination of the relationship between d_{33} and the relative density of ferroelectric lattices and foams. B) Loading state, and C) relationship between d_{33} and inclination angle θ of stretching and bending-dominated cross trusses. D) Scaling operation of octet truss. E) 3D contour map for d_{33} for alternative octet truss ferroelectric metamaterials. Influence of relative density and scaling ratio on the d_{33} of F) stretching-dominated octet truss, BCC, and SC, and G) bending-dominated tetrakaidecahedron, cross truss, and honeycomb cellular ferroelectric metamaterials. H) Optical view and measured d_{33} of representative octet truss ferroelectric metamaterials. I) Comparison among the maximum experimentally achievable d_{33} value of $BaTiO_3$ ceramics in this work through cellular ferroelectric metamaterial design and those reported in the literature.[9–11,28]

of porosity, resulting in a diminished piezoelectric response, tied to the decline in remnant polarization. This poor polarization is intricately associated with the electric field distribution within the porous ferroelectrics with complex underlying architecture.[26] In this research, a rational design of the microarchitecture of ferroelectric metamaterials unveils an unconventional behavior for d_{33}. **Figure** 2a illustrates the d_{33} values of the octet truss, tetrakaidecahedron, and five types of foams with varying relative density. Due to the structural disconnection at small ρ_r, the relative densities for these 3D-printed foams are kept above 0.3. Featuring well-developed mathematical foundations, the modified asymptotic homogenization considering the influence of polarization electric field is implemented to determine the effective piezoelectric and pyroelectric properties for the octet truss and tetrakaidecahedron with periodic boundary conditions (Section S2, Supporting Information), while a detailed finite element analysis is conducted for multiphysical analysis of random ferroelectric foams. Considering the intricate polarization electric field, the local element coordinates undergo adjustments according to the electric field determined by polarization simulation. Remarkably, the d_{33} value of the octet truss displays an unprecedented rise as the relative density decreases, ascending from 285 ± 5

pC N^{-1} measured for an octet truss with ρ_r = 0.5 to 347 ± 2 pC N^{-1} measured for an octet truss with at ρ_r = 0.1. Conversely, the d_{33} values for the bending-dominated tetrakaidecahedron and bending-dominated foams exhibit a marginal decline when ρ_r decreases.

The piezoelectric properties of the ferroelectric lattice and foams are fully activated; beyond polarization electric fields (> 1.5 kV mm^{-1}), there is no observed subsequent enhancement in d_{33} (Section S3, Supporting Information). The local polarization predominantly aligns with the strut orientation in the lattice-based ferroelectric metamaterials (Section S4, Supporting Information). In addition, it is the stress transfer or loading state that governs the distinct behaviors of ferroelectric metamaterials depicted in Figure 2a. In the case of representative stretching-dominated cross truss, as presented in Figure 2b, i.e., extracted from the octet truss, since the strut only experiences compressive or tensile deformation, the internal compressive force F_1 is determined as follows upon an external compression F:

$$F_1 = F/\sin\theta \quad (1)$$

However, for a bending-dominated cross truss extracted from a bending-dominated lattice, the compressive force F_1 is obtained by:

$$F_1 = F\sin\theta \quad (2)$$

Since $\sin\theta \leq 1$, the internal force F_1 within the metamaterial when subjected to a compressive force F is augmented for a stretching-dominated cross truss compared to a bending-dominated one, leading to an enhanced d_{33}. The relationship between effective $d_{33}^{\text{Stretching}}$ and d_{33}^{Bending}, inclined angle θ, and $d_{33,s}$ value of the constitutive ferroelectric material is given by (Section S5, Supporting Information):

$$\text{Stretching} - \text{dominated cross truss}: \; d_{33}^{\text{Stretching}} = d_{33,s}/\sin\theta \quad (3)$$

$$\text{Bending} - \text{dominated cross truss}: \; d_{33}^{\text{Bending}} = d_{33,s}\sin\theta \quad (4)$$

Verified by the asymptotic homogenization's result, Equation 3 demonstrates accuracy in predicting the effective d_{33} for both stretching and bending-dominated cross lattices as shown in Figure 2c. Since small θ leads to an increased intersection area of the two lattice struts, thus perturbing the distribution of the force and polarization direction, the divergence between the homogenization (blue dashed) and theoretical beam-model (solid line) results occurs when $\theta < 20°$. Therefore, based on Equation 3, the stretching-dominated octet truss ($\theta = 45°$) displays a higher d_{33} value than the bulk material. Additionally, decreasing ρ_r translates to a reduced intersection region among beams. Consequently, this facilitates a superior alignment of the force and polarization field with the beam direction, leading to an amplified d_{33} (Section S6, Supporting Information). Although the beam incline angles of inside tetrakaidecahedron and foams vary in space, their bending-dominated behaviors yield smaller d_{33} values compared to bulk materials, particularly evident at lower relative densities.

Inspired by Equation 3, we introduce a design strategy for low relative density ferroelectric metamaterials aimed at achieving exceptionally high piezoelectric charge constants. Illustrated in Figure 2d, scaling the octet truss along the polarization direction with a ratio of s allows us to adjust the truss's inclined angle, thereby enabling the attainment of the desired d_{33} value. As shown in Figure 2e, decreasing the relative density and scaling ratio corresponds to an augmentation in d_{33}, observed in both homogenization and experiment results. For example, the d_{33} value of the octet truss with $\rho_r = 0.3$ and $s = 1$ stands at 304 ± 3 pC N^{-1}, yet it is increased to 849 ± 11 pC N^{-1} for $\rho_r = 0.1$ and $s = 0.2$. The d_{33} contour map associated with the tetradecahedron truss with a contrasting trend is shown in Section S7, Supporting Information. The Young's modulus of these truss-based ferroelectric metamaterials is provided in Section S8 of the Supporting Information. To validate the versatility of the proposed ferroelectric design strategy, apart from the octet truss ($Z = 12$), Figure 2f also involves two other stretching-dominated lattices, i.e., BCC with Z = 8 and SC with Z = 6 that is stretching-dominated only along the three normal directions. Here, Z denotes the number of trusses connected to a single joint. Since its θ is insensitive to the scaling ratio, the SC maintains an almost constant d_{33} with varying s and ρ_r. Due to the high inclined angle ($\theta = 90°$) of the four vertical beams, BCC shows a smaller d_{33} than that of the octet truss. At smaller s values, a minor decrease in the d_{33} value of SC ferroelectrics is observed, induced by a greater distribution of loads among the vertical beams. In Figure 2g, three bending-dominated lattices, i.e., tetrakaidecahedron (Z = 4), cross truss (Z = 4), and honeycomb (Z = 3), exhibit distinctive trends where a decrease in both ρ_r and s results in a reduced d_{33} across these ferroelectric metastructures.

Figure 2h showcases representative octet truss ferroelectric lattices along with their measured d_{33} values. The limitations of the resorted DLP 3D printer restrict the maximum achievable d_{33} value of the octet truss family to 849 ± 11 pC N^{-1}, observed for $\rho_r = 0.1$ and $s = 0.2$. Nevertheless, the utilization of advanced 3D printing techniques,[19b,27] such as two-photon lithography (TPP), holds the promise of further amplifying this value by fabricating ferroelectric metamaterials with smaller relative densities and scaling ratios. As depicted in Figure 2i, our maximum measured d_{33} surpasses the corresponding values for $BaTiO_3$ ceramics achieved through material processing and sintering optimization reported in the literature,[9–11,28] such as microwave sintering and grain and domain engineering. Notably, the reported values in the literature pertain specifically to bulk $BaTiO_3$ ceramics and do not impart architected design strategy for enhancing the piezoelectric properties of lightweight ferroelectric ceramics (Section S9, Supporting Information); combining the architected material design strategy with those material composition/manufacturing-enabled enhancement of piezoelectric properties can further escalate the ranges of attainable d_{33} in next generation of ferroelectric materials. For example, the d_{33} value of solid $BaTiO_3$ ceramics can reach a maximum of 788 pC N^{-1} using the templated grain growth method;[9a] by utilizing this material as feedstock for 3D printing of octet truss ferroelectric materials (with $\rho_r = 0.1$, $s = 0.2$), the d_{33} value can be further enhanced by ≈3.3 times (Section S9, Supporting Information) to reach ≈2600 pC N^{-1}.

The piezoelectric voltage constant, denoted by g_{33}, is crucial in determining the electric field produced per unit of applied mechanical stress and is calculated as the ratio of the

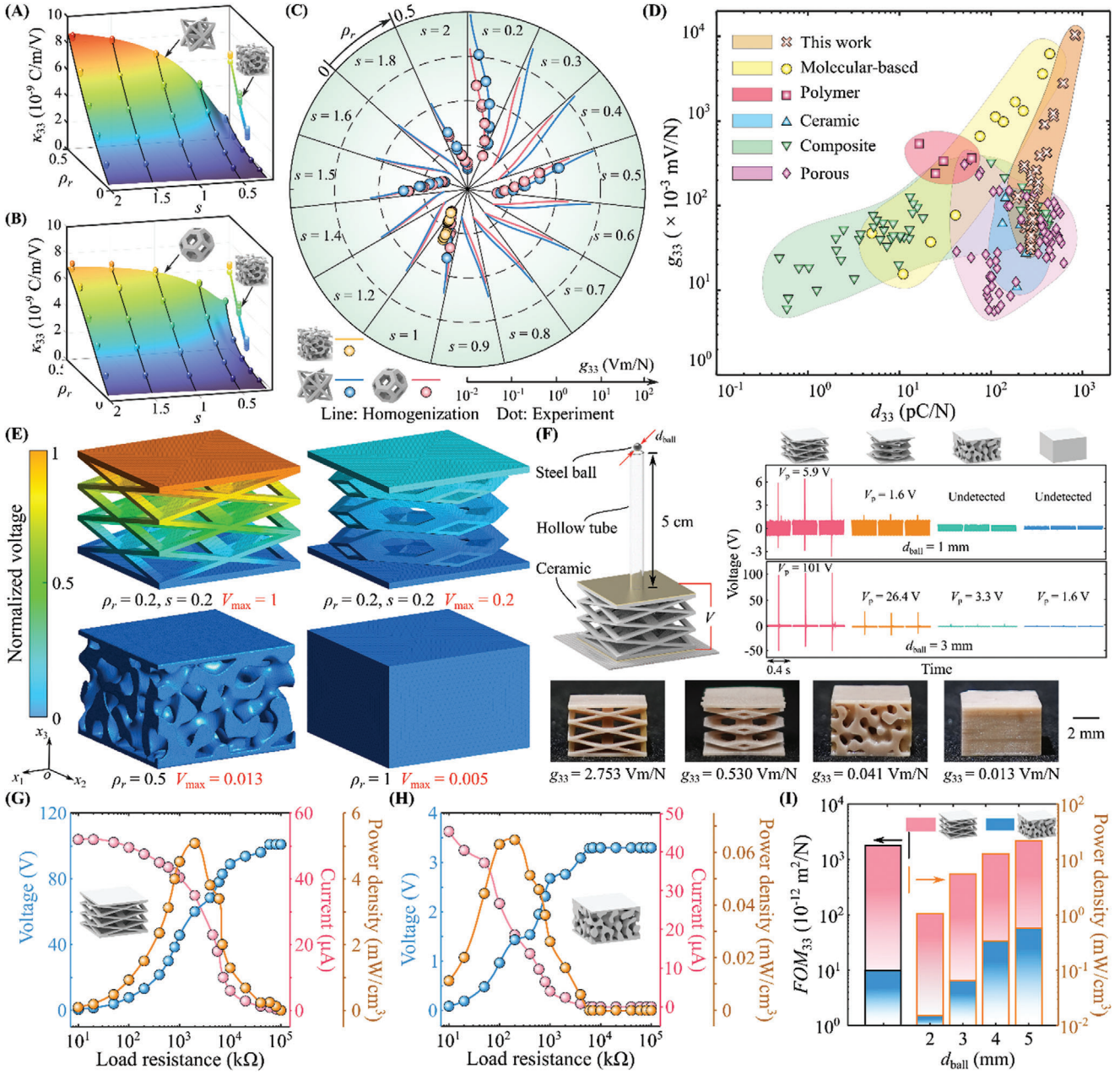

Figure 3. Piezoelectric voltage constant g_{33} of ferroelectric lattice metamaterials. Dielectric constant κ_{33} of A) octet truss and B) tetrakaidecahedron family lattices. C) Piezoelectric voltage constant g_{33} of ferroelectric lattices for alternative relative densities and scaling ratios. D) Comparison of d_{33} and g_{33} across architected ferroelectric lattices and reported ferroelectric materials (see Section S12, Supporting Information for reference and details). E) Simulation and F) experimental drop weight test of octet truss ($\rho_r = 0.2$ and $s = 0.2$), tetrakaidecahedron ($\rho_r = 0.2$ and $s = 0.2$), foam ($\rho_r = 0.5$), and fully solid ferroelectric ceramics. The output voltage, output current, and output power density of ferroelectric G) octet truss ($\rho_r = 0.2$, $s = 0.2$) and H) foam ($\rho_r = 0.5$) subjected to the drop of a 3 mm steel ball. I) Comparison of the figure of merit for energy harvesting (FOM_{33}) and power density under alternative drop ball sizes for the ferroelectric octet truss and foam metamaterials.

piezoelectric charge coefficient (d_{33}) to the dielectric constant (κ_{33}). Consequently, the dielectric constant of the ferroelectric lattices is first examined in **Figure** 3a,b. Unlike d_{33}, κ_{33} values for both the octet truss and tetrakaidecahedron family demonstrate a declining trend by decreasing relative density (ρ_r) and scaling ratio (s). Indeed, the decrease in ρ_r results in fewer materials to generate electric charges under a given external electric field. In addition, the decrease of s value implies a reduction in the local electric field experienced by inclined beams, resulting in lower electrical charge generated along x_3-direction per unit volume, i.e., κ_{33}. This decrease is proportional to the cosine value of the beam inclined angle (Section S10, Supporting Information). Hence, through the scaling operation, we can attain κ_{33} values significantly smaller than ferroelectric foams with the same ρ_r.

For instance, the mean κ_{33} values for 3D printed octet truss (s = 0.2) and tetrakaidecahedron (s = 0.2) with ρ_r = 0.5 are 1.49 and 3.68 nC m^{-1} V^{-1}, respectively, whereas 6.21 nC m^{-1} V^{-1} for the foam and 20.36 nC m^{-1} V^{-1} for the solid $BaTiO_3$ piezoceramic, measured by an LCR meter (SR 715, Stanford Research Systems, USA) at 1 kHz.

As presented in Figure 3c, the underlying topology, scaling ratio, and relative density play pivotal roles in determining the piezoelectric voltage constant. A notable outcome of the significant reduction in κ_{33} is the amplification of g_{33} with the decrease of ρ_r and s. For instance, in ferroelectric foam structures, the mean g_{33} rises from 0.0412 to 0.139 Vm N^{-1} as ρ_r decreases from 0.5 to 0.3, whereas g_{33} is 0.013 Vm N^{-1} for solid ferroelectric materials. Similarly, for octet truss and tetrakaidecahedron structures with ρ_r of 0.3, the mean g_{33} value increases from 0.093 and 0.070 to 0.968 and 0.352 Vm N^{-1}, respectively, as the scaling ratio diminishes from 1 to 0.2. The influence of ρ_r and s on the d_{33} can be found in Figure 2. In bending-dominated tetrakaidecahedron structures, a decrease in ρ_r and s leads to a moderate decline in d_{33} whereas a more substantial reduction in κ_{33} noticeably boosts g_{33}. For instance, when ρ_r decreases from 0.5 to 0.3, the average d_{33} of tetrakaidecahedron (s = 1) drops from 256 to 238 pC N^{-1} (Figure S13, Supporting Information), accompanied by a decrease in κ_{33} from 6.19 to 3.39 nC m^{-1} V^{-1} (Figure 3b). Consequently, g_{33} increases from 0.041 to 0.070 Vm N^{-1} (Figure 3c). Notably, in conventionally manufactured porous ferroelectric ceramics, high porosity leads to a considerable decrease in d_{33}, offsetting the benefits gained from the decreased κ_{33}.[12b–e] Nevertheless, d_{33} still maintains a reasonable value despite a small relative density in our 3D-printed bending-dominated lattices and foams. Conversely, for stretching-dominated octet truss structures, d_{33} demonstrates an increasing trend with the decrease of ρ_r and s, while κ_{33} shows the opposite trend, allowing us to achieve ultrahigh g_{33} values in architected ferroelectric metamaterials. For instance, the mean g_{33} increases from 0.0319 to 11.098 Vm N^{-1} for octet truss when ρ_r and s decreases from 0.5 and 2 to 0.1 and 0.2, respectively.

High values of d_{33} and g_{33} are essential for various piezoelectric applications as sensors, actuators, and energy harvesters. However, achieving materials with both high d_{33} and g_{33} simultaneously has posed a longstanding challenge, as an increase in d_{33} is typically accompanied by a decrease in g_{33}. As depicted in Figure 3d, piezoceramics often exhibit a high d_{33} value (100–400 pC N^{-1}) but lack competitive g_{33} (0.01–0.13 Vm N^{-1}) due to their high dielectric constant. Introducing a second phase, such as polymer for composite ferroelectrics or voids for porous ferroelectrics, presents an effective strategy to enhance mechanical flexibility and as a result g_{33}, albeit at the cost of reduced d_{33}. For instance, in a referenced study,[29] d_{33} of ferrocomposite decreases from 438 to 219 pC N^{-1} accompanied by an increase in g_{33} from 0.065 to 0.157 Vm N^{-1}. Similarly, ferroelectric polymers like polyvinylidene fluoride (PVDF) offer a balanced compromise between d_{33} (16–62 pC N^{-1}) and g_{33} (0.3–0.5 Vm N^{-1}).[30] Recent advancements in tailoring the chemical constituents of molecular-based ferroelectric materials have shown promise in achieving high values of both d_{33} and g_{33}.[31] For instance, a hybrid perovskite ferroelectric, $[Me_3NCH_2Cl]$-$CdBrCl_2$, demonstrated remarkable d_{33} and g_{33} values of 440 pC N^{-1} and 6.215 Vm N^{-1}, respectively.[31a] By finely tuning the microarchitecture of ferroelectric metamaterials, our present work can simultaneously achieve ultrahigh d_{33} (849 pC/N) and g_{33} (11.098 Vm N^{-1}) even when utilizing relatively weak ferroelectric ceramics (i.e., $BaTiO_3$). Moreover, the architected material design approach presented here for piezoelectric materials is independent of their constitutive solid base materials and has no theoretical boundary for both d_{33} and g_{33} where a simultaneous reduction of ρ_r and s in stretching-dominated lattice piezoelectric materials may lead to infinitely high values.

Figure 3e presents the simulation results for the octet truss (ρ_r = 0.2 and s = 0.2), tetrakaidecahedron (ρ_r = 0.2, s = 0.2), foam (ρ_r = 0.5), and solid piezoelectric materials. To evenly distribute the force, two thin plates are incorporated at the top and bottom of these cellular materials to experience the compression force. As anticipated, the octet truss exhibits the highest normalized voltage of 1, surpassing that of tetrakaidecahedron, foam, and fully solid ferroelectric materials by factors of 5, 77, and 200, respectively, owing to its ultrahigh g_{33} value. Each of these four structures is 3D printed and then subjected to a drop-weight test using a steel ball dropped from a 5 cm height. Upon impact by a small ball (diameter of 1 mm), the voltage responses for foam and solid materials are undetectable while 5.9 and 1.6 V responses are found for octet truss and tetrakaidecahedron, respectively. Subsequently, when impacted by a ball with a diameter of 3 mm, the octet truss yielded an average voltage response of 101 V, significantly greater than the other three designs. This observation aligns with the superiority of the octet truss results found by numerical simulation of the drop weight test results and by experimental measurement of g_{33} value (i.e., 2.753 Vm N^{-1} for octet truss) (see Video S1, Supporting Information). In addition to high sensitivity, our ferroelectric metamaterials also demonstrate a fast response time of around 0.2 ms (see Section S11, Supporting Information).

To validate the energy harvesting performance of the rationally designed ferroelectric lattices, the voltage, current, and power density across varying load resistance for ferroelectric octet truss and foam are measured and compared in Figure 3g,h. For the measurement, the diameter of the dropped steel ball is first kept at 3 mm. With the increase of load resistance, the voltage increases while the current gradually decreases, and the power density peaks at 2 MΩ and 200 kΩ, respectively, with corresponding values of 5.09 and 0.06 mW cm^{-3} for octet truss and foam ferroelectrics. As presented in Figure 3i, the advantage observed for generated power density persists across alternative drop weights. This is attributed to the elevated figure of merit for piezoelectric energy harvesting (FOM_{33}), which evaluates electrical energy density under mechanical stress and is calculated as $d_{33}^2/\kappa_{33}^{\sigma}$. Specifically, the experimentally measured FOM_{33} values for octet truss and foam are 1762×10^{-12} and 10×10^{-12} m^2 N^{-1}, respectively.

As presented in **Figure** 4a, to expand the design space for acquiring diverse transverse piezoelectric constants (d_{31} and d_{32}), scaling operation is performed along both x_1-direction and x_3-direction, with a scaling ratio of s_1 and s_3, respectively. Alternative combinations of these two scaling ratios (ranging from 0.2 to 2) and relative density (ranging from 0.05 to 0.5) are explored for ferroelectric octet truss and tetrakaidecahedron. The (d_{31}, d_{32}) values for a total of 1453 distinctive topologies of ferroelectric lattices and foams are presented in Figure 4b. Apart from

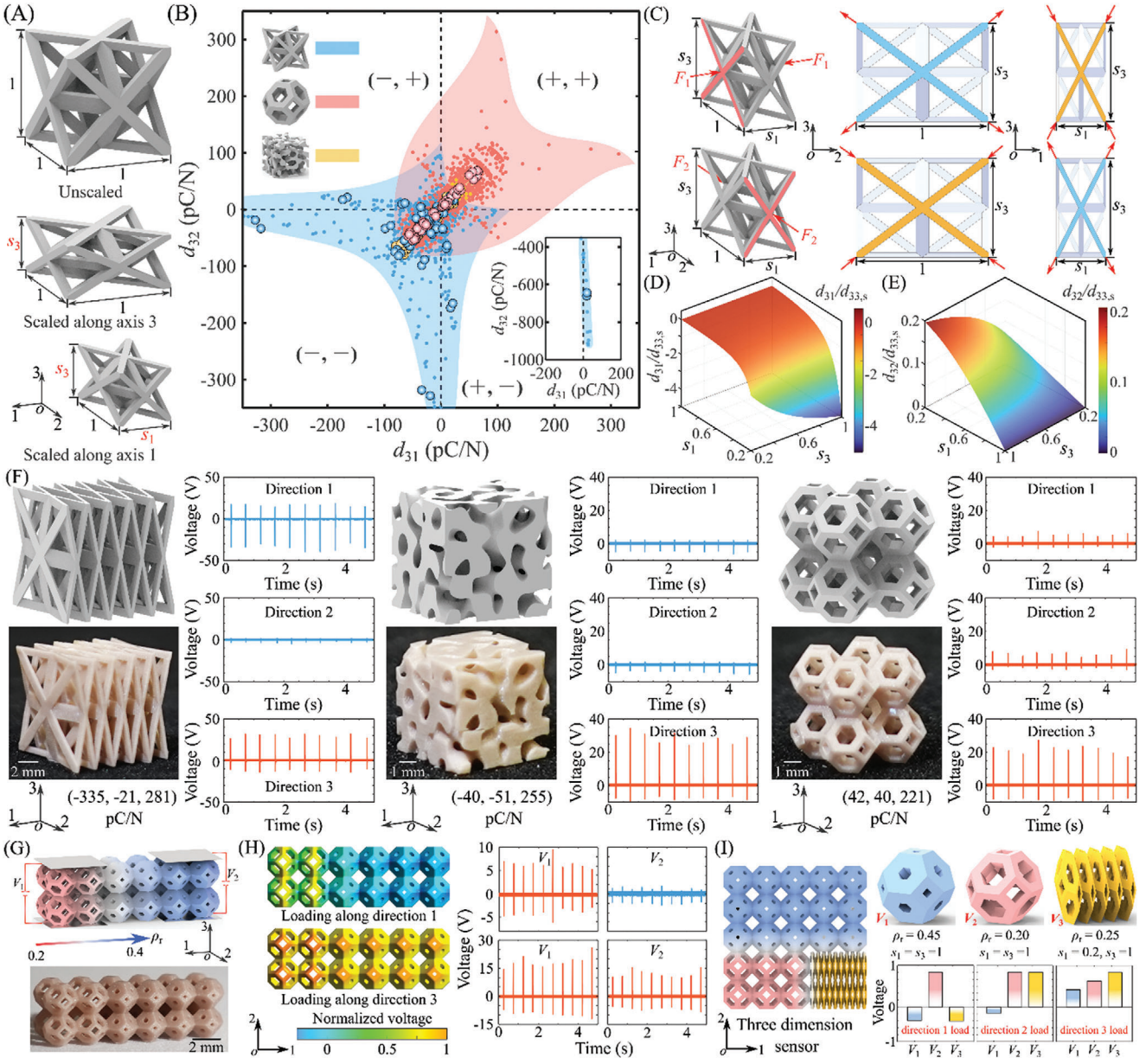

Figure 4. Transverse piezoelectric charge constant of ferroelectric lattice metamaterials. A) Scaling operation of lattices along x_1-direction and x_3-direction. B) Numerical (small dots) and experimental (big dots) d_{31} and d_{32} of octet truss and tetrakaidecahedron family lattices and foam. C) Loading states of a ferroelectric octet truss compressed under x_1-direction and x_2-direction. Theoretical D) d_{31} and E) d_{32} contour maps of ferroelectric octet truss concerning varying s_1 and s_3. F) Voltage responses of ferroelectric octet truss, foam, and tetrakaidecahedron with representative transverse piezoelectric anisotropies. G) One-direction-graded tetrakaidecahedron, and its H) simulation and experimental local voltage response, when compressed in x_1-direction and x_3-direction compression. I) A 3D force sensor made of a two-direction-graded tetrakaidecahedron and its local voltage response.

the samples printed in Figure 3c, additional octet truss with ρ_r of 0.1 and 0.2, and (s_1, s_3) of (0.2, 1), (0.4, 1), (0.6, 1), and (0.8, 1), are fabricated. Interestingly, (d_{31}, d_{32}) of our designed ferroelectric lattices exhibit a broad range of values across all four phases, greatly expanding the range of transverse piezoelectric anisotropies. In specific, most (d_{31}, d_{32}) of the tetrakaidecahedron family fall within the first phase while those of the octet truss family are primarily found in the third phase. For instance, without scaling operation ($s_1 = s_3 = 1$), the experimental d_{31} and d_{32} values for the tetrakaidecahedron structures range from 57 to 12 pC N^{-1}, while for the octet truss structures, vary from −5 to −22 pC N^{-1} as the relative density changes from 0.1 to 0.3. It is noted that by engineering the scaling operation, we can achieve ultrahigh values for the magnitude of d_{31} and d_{32}. For example, the mean experimental d_{31} value of octet truss with (ρ_r, s_1, s_3) of (0.1, 0.2, 1) reaches −659 pC N^{-1}, 6.00 and 2.44 times higher than the magnitude of d_{31} (−110 pC N^{-1}) and d_{33} (270 pC N^{-1}) values of the solid ferroelectric materials, respectively. Similarly, for tetrakaidecahedron, we can also achieve an ultrahigh theoretical d_{31} value of 313 pC N^{-1} with geometrical parameters (ρ_r, s_1, s_3) adjusted to (0.05,

0.2, 2). Opposed to lattice ferroelectrics, the (d_{31}, d_{32}) of ferroelectric foams is located in phase III (−, −), and decreases rapidly in terms of magnitude by decreasing relative density.[12e] Although diverse combinations of d_{31} and d_{32} can also be achieved in by spinodal ferroelectrics,[24] their magnitude is limited to the d_{31} and d_{32} value of the constitutive solid ferroelectric material.

The remarkable transverse piezoelectric properties exhibited by our ferroelectric lattices stem from their intrinsic microarchitectures. To analyze the d_{31} and d_{32} of octet truss, compressive forces along x_1-direction and x_2-direction are applied as shown in Figure 4c where blue beams experience tension states while orange beams experience compression states, both contributing to charge generation for d_{31} and d_{32}. Like the theoretical analysis of d_{33}, the force acting on the inclined beams of a lattice dominated by stretching can be intensified, thereby amplifying the corresponding electric charge component along x_3-direction, and thus resulting in exceptionally high d_{31} values for stretching-dominated octet truss ferroelectric structures with low relative density, The relationship between d_{31} and d_{32} with the two scaling ratios can be expressed as follows (derivation can be found in Section S13, Supporting Information):

$$d_{31} = \frac{s_3\left(\sqrt{s_1^2+s_3^2} - \sqrt{1+s_3^2}\right)}{2s_1^2} d_{33,s} \tag{5}$$

$$d_{32} = \frac{s_3\left(\sqrt{1+s_3^2} - \sqrt{s_1^2+s_3^2}\right)}{2} d_{33,s} \tag{6}$$

Based on Equation 4, the impact of s_1 and s_3 on d_{31} and d_{32} is illustrated in Figure 4d,e. The magnitude of d_{31} shows an increasing trend with decreasing s_1 and increasing s_3. Since d_{31} is inversely proportional to s_1, we can attain a high $d_{31}/d_{33,s}$ ratio by reducing s_1. Conversely, d_{32} features small values compared to d_{31}.

In the meantime, for bending-dominated tetrakaidecahedron ferroelectrics with low relative density with scaling ratios of unity, the d_{31} and d_{32} can be given as:

$$d_{3i} = \frac{d_{33,s}}{2\sqrt{2}} \ (i = 1,\ 2) \tag{7}$$

This relationship elucidates the positive values of d_{31} and d_{32} observed in tetrakaidecahedron structures with low relative density. The remarkably high value of the three piezoelectric constants and exceptionally small dielectric constant of the ferroelectric lattices contribute significantly to enhancing the performance of the hydrophone devices (refer to Section S14, Supporting Information).

Figure 4f presents the voltage responses of ferroelectric lattices and foam with three representative transverse piezoelectric anisotropies under uniaxial compressive impacts along three directions. Specifically, the geometrical parameters (ρ_r, s_1, s_3) for the octet truss and tetrakaidecahedron ferroelectric structures are (0.2, 0.2, 1) and (0.2, 1, 1), respectively, while the relative density of the foam is 0.6. Due to the notably high absolute value of d_{31} (−335 pC N^{-1}), the voltage response of the octet truss loaded in x_1-direction surpasses that loaded in x_3-direction 3. Introducing porosity results in a smaller d_{31} and d_{32} for ferroelectric ceramics, thereby causing considerably smaller voltage responses along x_1-direction and x_2-direction loading compared to the x_3-direction. Conversely, since all three piezoelectric constants share the same sign, the voltage response of the tetrakaidecahedron structure exhibits the same sign when compressed along all three orientations (see Video S2, Supporting Information).

The diverse transverse piezoelectric anisotropies enable the design of integrated force directionality sensors. Illustrated in Figure 4g, a one-directional graded tetrakaidecahedron, comprised of two relative densities of 0.2 and 0.4 without scaling operation, demonstrates a programmable local voltage response. For $\rho_r = 0.2$, d_{31} and d_{32} in tetrakaidecahedron are positive whereas they are negative for $\rho_r = 0.4$. Consequently, under compression along x_1-direction, the voltage signs of two local electrodes, i.e., V_1 and V_2 differ, while due to the same sign of d_{33} for both cells, the signs of V_1 and V_2 under x_3-direction loading are the same. This functionality is verified through both simulation and experimentation (Figure 4h). To further distinguish the force direction among x_2-direction and x_3-direction, a new type of tetrakaidecahedron with (ρ_r, s_1, s_3) of (0.25, 0.2, 1) is introduced in a two-directional graded design, whose d_{31} is positive while d_{32} is negative. As presented in Figure 4i, by analyzing the voltage signs of these three local electrodes, we can determine the force orientation applied in this integrated sensor.

Apart from d_{31}, d_{32}, and d_{33}, d_{42}, and d_{51} are also considerable nonzero piezoelectric constants for shear-based piezoelectric devices, linking the shear stresses σ_4 and σ_5 to the electric charges D_2 and D_1, respectively. Inspired by the unprecedentedly large values of d_{3i} (i = 1, 2, 3) shown in Figures 2 and 4, we explore the influence of scaling operations (only along x_3-direction) and relative density on d_{42} (equivalent to d_{51}) for both ferroelectric octet truss (**Figure 5a**) and tetrakaidecahedron (Figure 5b) structures. Like the behavior of d_{33} in the octet truss, decreasing the scaling ratio increases d_{42}. Furthermore, for small values of s, reducing the relative density can further enhance d_{42}. For instance, the measured d_{42} of the octet truss ($\rho_r = 0.5$) increases from 371 to 499 pC N^{-1} as the scaling ratio (s) decreases from 2 to 0.2. This value is further enhanced to 836 pC N^{-1} in the octet truss with ρ_r = 0.1 and s = 0.2. Conversely, although the bending-dominated tetrakaidecahedron structure exhibits a weakened d_{33}, which decreases with both reduced ρ_r and s (as shown in Figure S10, Supporting Information), the d_{42} value demonstrates a different trend concerning these two design factors. Notably, for small relative density and scaling ratio, d_{42} of ferroelectric tetrakaidecahedron structure even displays higher values compared to the solid structure. For example, the experimental values of d_{42} are 572 and 621 pC N^{-1} for the tetrakaidecahedron structure with (ρ_r, s) of (0.2, 0.2) and (0.2, 0.1), respectively, which are 36% and 48% higher than those of solid $BaTiO_3$ ceramic ($d_{42,s}$ = 420 pC N^{-1}).

The behavior can be explained by the load state illustrated in Figure 5c. For simplification, consider the cross truss: one end of the two beams is fixed while the other end is subjected to a downward force, F. If these two beams are under stretching-dominated conditions, the force component along the beam direction, F_1, is:

$$F_1 = F/\sin\theta \tag{8}$$

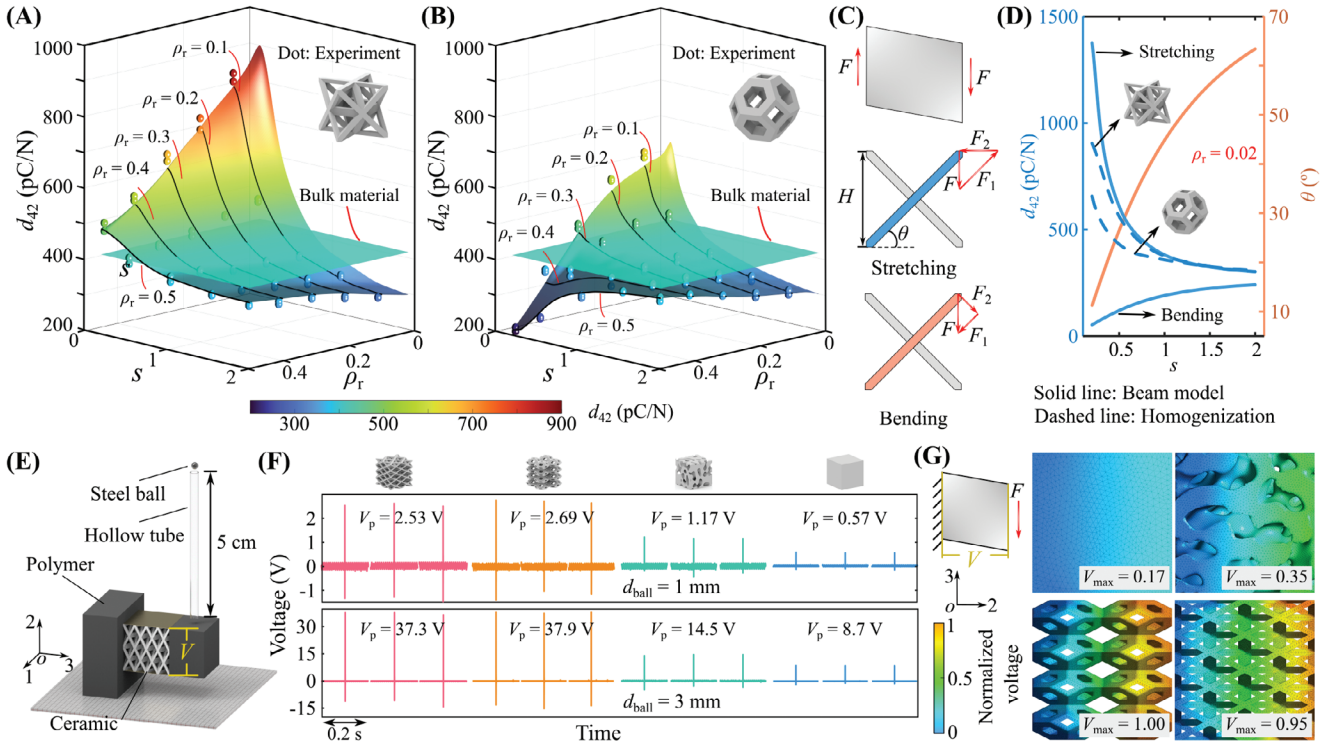

Figure 5. Shear-mode piezoelectric properties of ferroelectric lattice metamaterials. Effective d_{42} of ferroelectric A) octet truss and B) tetrakaidecahedron lattices for alternative relative densities and scaling ratios. C) Loading state, and D) relationship between d_{42} and the inclination angle θ of stretching- and bending-dominated cross trusses. E) Drop weight test setup, F) experimental voltage response, and G) simulation results for the ferroelectric solid, lattices, and foam based on shear-mode piezoelectric properties.

and thus the effective d_{42} for this stretching-dominated cross truss is:

$$d_{42} = d_{33,s}/\sin\theta \tag{9}$$

Similarly, for a bending-dominated cross truss, the effective d_{42} is

$$d_{42} = d_{33,s}\sin\theta \tag{10}$$

Comparing Equations 9 and 10 with Equations 3, it is evident that both the effective d_{42} and d_{33} for bending- and stretching-dominated trusses share the same value at small relative densities, as predicted by the beam model. The theoretical upper and lower bounds for d_{42} derived from Equations 9 and 10 are illustrated in Figure 5d. Decreasing the scaling ratio results in a reduced inclined angle θ, which in turn increases d_{42} for stretching-dominated cross trusses (upper boundary) and decreases d_{42} for bending-dominated cross trusses (bottom boundary). For the octet truss with ρ_r of 0.02, the homogenization result approaches the upper boundary. For a bending-dominated tetrakaidecahedron structure ($\rho_r = 0.02$), the homogenization result is also closer to the upper boundary. This can be attributed to the fact that, under the shear mode, a portion of the tetrakaidecahedron structure is subjected to stretching-dominated conditions (Section S15, Supporting Information), thereby exhibiting a combination of stretching and bending-dominated behaviors.

Decreasing ρ_r also leads to a reduction in the dielectric constants κ_{11} and κ_{22}. Therefore, the enhanced d_{42} and d_{51}, along with the decreased κ_{11} and κ_{22}, contribute to the improved g_{42} ($= d_{42}/\kappa_{22}$) and g_{51} ($= d_{51}/\kappa_{11}$), indicating increased sensitivity to a shear force. Figure 5e illustrates the setup for the shear-mode-based piezoelectric test, in which one side of the lattices along the polarization direction is fixed to a 3D printed polymeric block by glue, while the other side is attached to another block to bear the impact load imposed by a steel ball dropped from a height of 5 cm. Four ferroelectric structures are considered: tetrakaidecahedron and octet trusses ($\rho_r = 0.3$, $s = 0.5$), random foam ($\rho_r = 0.6$), and a solid block with overall dimensions of 6.3 × 6.3 × 6.3 mm. As depicted in Figure 5f, the voltage responses of both architected ferroelectric lattices are ≈2.4 and 4.4 times higher than the corresponding values for the ferroelectric foam and solid structures, respectively, under two different drop heights (Video S3, Supporting Information). Numerical simulation also confirms the superiority of the designed ferroelectric lattice for shear-mode piezoelectricity (Figure 5g).

Besides the piezoelectric effect (*electromechanical coupling*), polarized ferroelectric materials also exhibit the pyroelectric effect (*thermoelectric coupling*). As shown in **Figure 6a**, the spontaneous polarization or orientation of electric dipoles changes with temperature fluctuations, releasing charges on the surface of the ferroelectric material. The pyroelectric constant, p_3, defined as the generated electric charge per unit area per unit temperature change, assesses the pyroelectricity of the ferroelectric material. Figure 6b presents the p_3 values of ferroelectric octet truss

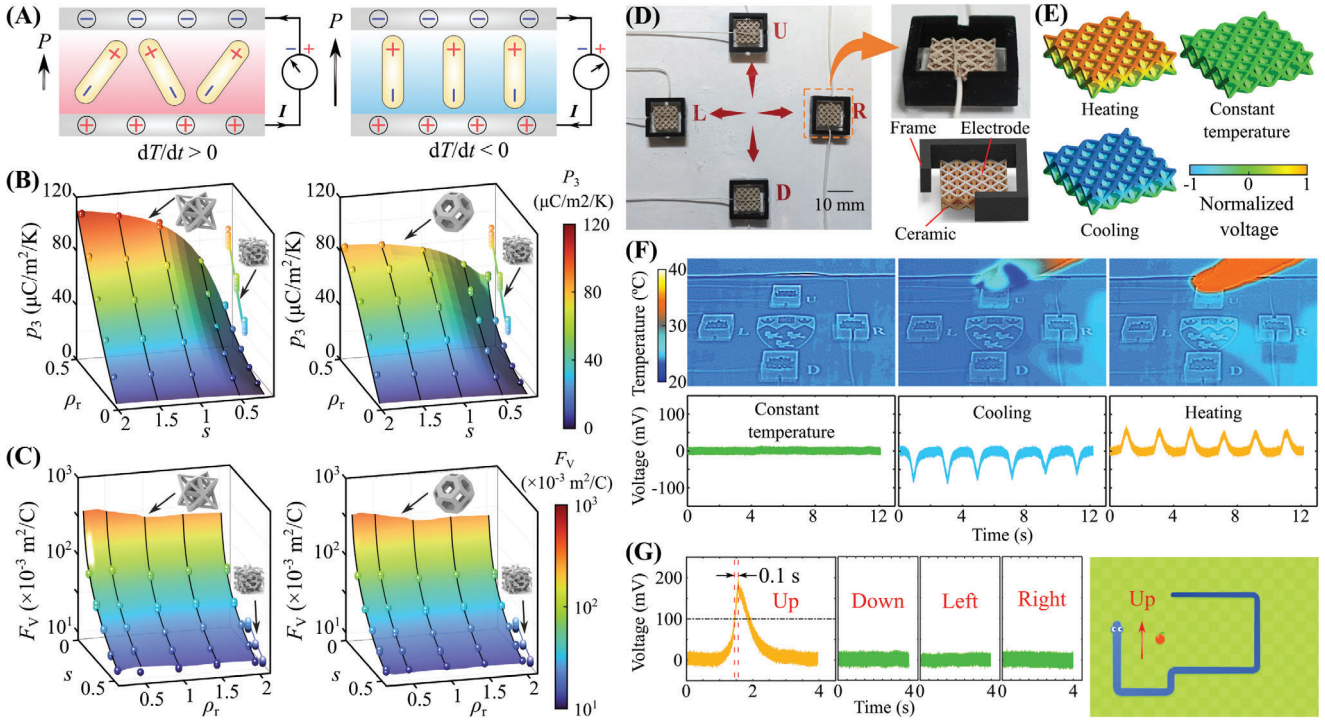

Figure 6. Pyroelectric properties of ferroelectric lattice metamaterials. A) Mechanism of the pyroelectricity. B) Pyroelectric constant and C) pyroelectric voltage responsivity of ferroelectric octet truss and tetrakaidecahedron lattices. D) Touchless game control panel. E) Simulated pyroelectric voltage distribution of ferroelectric octet truss under cooling and heating conditions. F) Temperature profile and voltage response of a cold finger and a normal finger approaching the ferroelectric metamaterial element. G) Voltage responses for the upward motion in snake game.

and tetrakaidecahedron structures with alternative relative densities and scaling ratios where a decrease in ρ_r and s results in a weakened pyroelectric constant. The pyroelectric constant is also experimentally measured by a PolyK pyroelectric test system, with a heating rate of 2 °C min^{-1} from 30 to 50 °C. This is because lower ρ_r means less material is available to generate charges under given temperature fluctuations, and a decrease in s results in fewer charge components along the polarization direction. It is noted that for the scaling operation of unity, octet truss, tetrakaidecahedron structures, and random foam exhibit close values, ≈50 μC m^{-2} K^{-1} when $\rho_r = 0.3$.

To evaluate the voltage sensitivity of ferroelectric materials under a given power input, the pyroelectric voltage figure of merit, F_v, is defined as $F_v = p_3/(c_E \kappa_{33})$ where c_E represents the volume-specific heat capacity. As depicted in Figure 6c, independent of scaling ratio and structural topology, F_v is mainly determined by the relative density of ferroelectric lattices. For instance, with $\rho_r = 0.3$, F_v values for the ferroelectric octet truss are 17.9 × 10^{-3} and 18.1 × 10^{-3} m^2 C^{-1} for $s = 1$ and $s = 2$, respectively. In contrast, when $s = 1$, this value increases significantly from 10.7 × 10^{-3} to 56.7 × 10^{-3} m^2 C^{-1} as ρ_r decreases from 0.5 to 0.1. This is because although p_3 decreases with the reduced ρ_r and s, κ_{33} exhibits a similar pattern. Furthermore, since c_E is proportional to ρ_r, decreasing relative density effectively contributes to a substantial increase in F_v.

Utilizing the pyroelectric effect, we develop a contactless game control panel for the snake game, as shown in Figure 6d. The frame is higher than the ferroelectric octet truss ($\rho_r = 0.4$, $s = 1$, and overall size of 9.4 × 9.4 × 2.3 mm) to prevent direct contact between the finger and the ferroelectric sensor. Simulation results in Figure 6e demonstrate distinctive voltage distributions of the designed ferroelectric lattice under cooling and heating conditions. Figure 6f displays the response of the ferroelectric sensor at room temperature (24 °C) when approached by a cooled finger versus a normal finger. The opposite voltage signals under cooling and heating conditions confirm that the generated voltage is due to the variation of temperature, i.e., the pyroelectric effect. Figure 6g depicts the voltage responses of the four ferroelectric sensors when a finger approaches the "Up" direction sensor. When the voltage exceeds 100 mV, this sensor triggers the upward movement of the snake in the right figure, while the other three unselected sensors remain inactive. Additionally, a 0.1-s gap before activation ensures a rapid response in the snake's movement during operation. (Video S4, Supporting Information).

The distinctive responses of ferroelectric materials to external mechanical loads facilitate their application in wearable input devices. As illustrated in **Figure 7a**, shear-mode piezoelectricity results in opposing positive and negative voltage signals, i.e., V_1, between two surfaces when shear forces act along x_2-direction in the positive and negative directions. In contrast, compression along x_3-direction yields a positive voltage (V_2) between surfaces in x_3-direction. Capitalizing on these features, we have developed wearable sensors with slide mode and press mode functionalities, as depicted in Figure 7b, which exploit both shear-mode and compression-mode piezoelectric effects. In specific, a 2 × 2 × 2 octet truss with size of 4.8 × 4.8 × 4.8 mm and a relative density of 0.4 is selected to fabricate the ferroelectric sensor. In slide mode, as the sensor moves along the one-way grid panel,

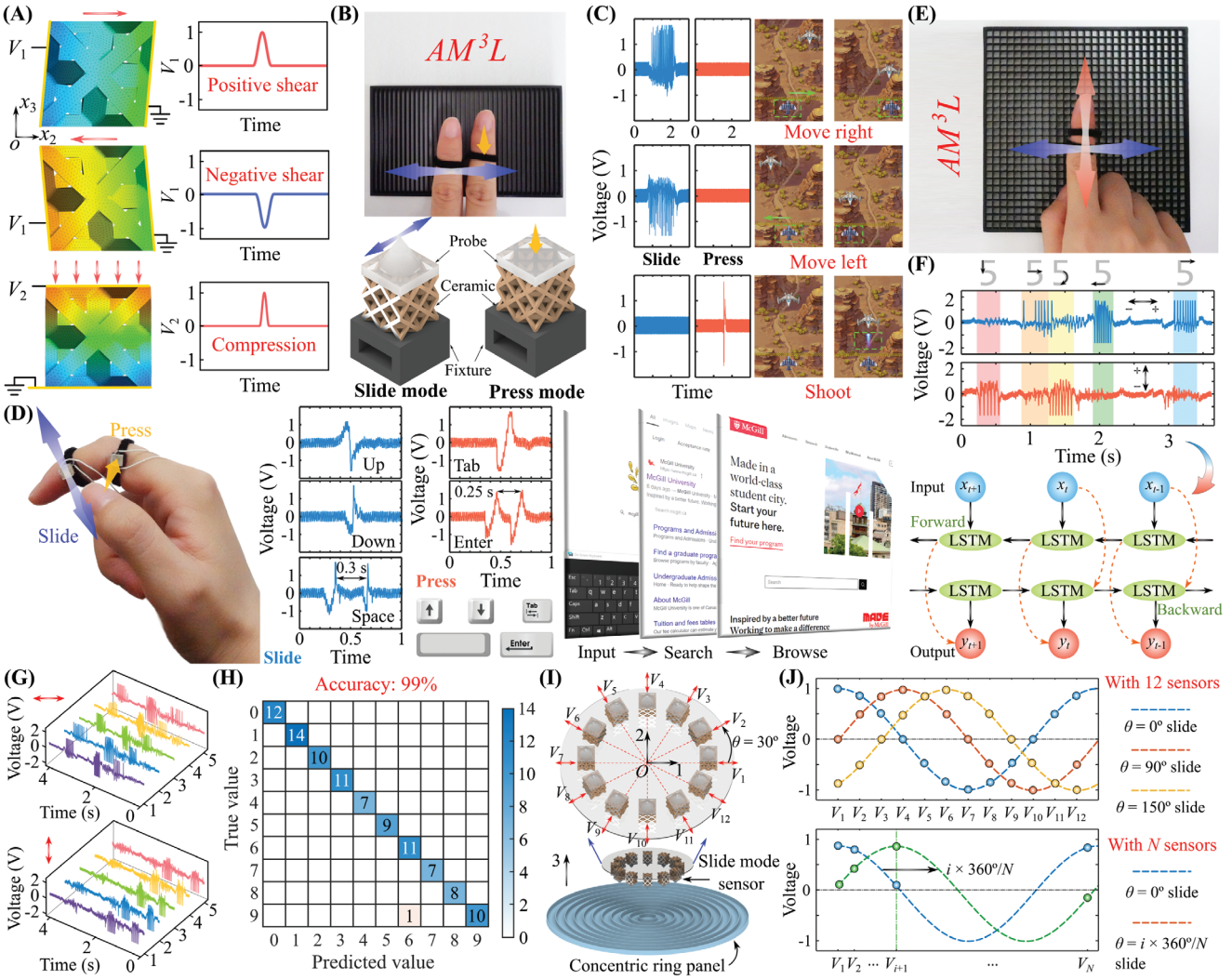

Figure 7. Wearable input devices based on ferroelectric metamaterials. A) Voltage responses of ferroelectric metamaterials under different shear and compressive loads determined by finite element simulation. B) Wearable game control setup with one-way grid panel featuring slide mode and press mode sensors. C) Commands and their corresponding voltage inputs. D) Wearable webpage interactive device simulating five keyboard functions. E) Wearable handwriting device with two slide mode sensors. F) Representative voltage signals for digit '5' and the bidirectional LSTM network used for recognition. G) Repeated voltage signals for handwriting digit '5'. H) Confusion matrix for handwriting recognition of digits from '0' to '9'. I) Setup configuration and J) voltage response analysis for precise detection of movement directions. Permission is granted to use the McGill website screenshot in Figure 7d and Video S7 (Supporting Information).

the applied shear force due to the contact between the soft probe tip and beams of the grid generates a voltage, whose polarity depends on the direction of the movement (Figure 7c). In the press mode, compression of the sensor produces a voltage pulse. Like game consoles, these sensors can be utilized to control actions during gaming, such as the movement and shooting of an airplane (Video S5, Supporting Information). In addition to game control, this wearable device is capable of simulating keyboard functions, thereby enabling interaction with webpages. As illustrated in Figure 7d, different sliding directions of the finger over the slide mode sensor generate opposing voltages, corresponding to the "Up" and "Down" arrow keys. A single compression of the press mode sensor signifies the "Tab" function. A double activation of these piezoelectric sensors with slide and compression modes denotes the "Space" and "Enter" commands, respectively. Thus, by utilizing the thumb and wearable sensors, users can efficiently perform inputs, searches, and web browsing (Video S6, Supporting Information).

Since a single slide mode sensor can detect two movement states (forward and backward) along one direction, employing two sensors of this type allows for the detection of four distinctive movement states across two orthogonal directions. By analyzing the output voltages corresponding to finger movements over a two-way grid panel, handwritten letters can be recognized (Figure 7e). Figure 7f illustrates the representative piezoelectric voltages for digit "5", recorded from two channels representing the horizontal and vertical directions, respectively. Correspondence between finger movement and voltage generation can be found, which is essential for effective handwriting recognition. For example, the initial and final strokes correspond to

downward and rightward movements, resulting in negative voltages for the vertical direction sensor and positive values for the horizontal direction sensor, respectively. To achieve real-time recognition of handwriting digits, each of them is repeated 50 times and used to train a bidirectional long short-term memory (LSTM) network, which leverages information from both past and future contexts, enhancing the understanding and capturing of long-range dependencies.[32] Figure 7g presents five of the output voltages for repeated handwriting for digit "5". The similar patterns observed from these two slide mode sensors demonstrate the reliability of the designed setup, resulting in 99% accuracy on the test dataset containing 100 cases (Figure 7h). Details on the implementation of handwriting recognition are provided in Section S16 and Video S7, Supporting Information.

To detect more movement directions, twelve slide mode ferroelectric metamaterials are arranged in a circular pattern with an angular separation of 30°; a concentric ring panel is designed to apply shear force through contact with the probe tip during finger movement (Figure 7i). As shown in Figure 7j, by analyzing the magnitudes of the output voltages from these twelve sensors, the movement direction can be determined. For instance, when moving along $\theta = 90°$, sensors V_1 and V_7 display voltages close to 0, while sensors V_4 and V_{10} exhibit maximum and minimum values, respectively, indicated by the orange line. Increasing the number of sensors can further enhance the direction sensitivity of the wearable device, where N movement states can be determined with N slide mode sensors, desired for applications such as advanced gesture recognition, nuanced control in virtual and augmented reality, and precise input for robotic systems.

3. Conclusion

In summary, we have proposed a strategy to develop truss-based ferroelectric metamaterials with ultrahigh piezoelectricity, diverse anisotropic piezoelectric properties, and exceptional ferroelectric figures of merit, all driven by their underlying microarchitecture. While introducing porosity typically reduces piezoelectricity in porous ferroelectrics, stretching-dominated truss-based lattices achieve remarkable improvements. At a relative density of 0.1, the d_{31} (or d_{32}), d_{33}, d_{42} (or d_{51}) values can reach 849, 659, and 836 pC N^{-1}, respectively—3.14, 6, and 2 times higher than its solid counterpart. The bending-dominated ferroelectric tetrakaidecahedron demonstrates promising piezoelectric anisotropy with a positive combination of (d_{31}, d_{32}, d_{33}) values, resulting from distinctive local polarization directions and force distribution patterns. Additionally, the dielectric constants decrease with reduced scaling ratio and relative density, leading to significantly enhanced ferroelectric figures of merit. For example, from the octet truss family, the piezoelectric voltage constant, piezoelectric energy harvesting figure of merit, and pyroelectric voltage sensitivity can reach 11.098 Vm N^{-1}, 9422 × 10^{-12} m^2 N^{-1}, and 56.7 × 10^{-3} m^2 C^{-1}, respectively. We deem our programmable multifunctional ferroelectric lattice metamaterials to offer versatile applications, spanning energy-absorbing structures, ultrasensitive force/thermal sensors, wearable self-powered input devices, and precisely controlled microelectromechanical systems.

Supporting Information

Supporting Information is available from the Wiley Online Library or from the author.

Acknowledgements

A.H.A. acknowledges the financial support by the Canada Research Chairs program in Multifunctional Metamaterials, Natural Sciences and Engineering Research Council of Canada through NSERC Discovery Grant (RGPIN-2022-04493), and Canada Foundation for Innovation (CFI) through John R. Evans Leaders Fund. A.H.A., V.O., and A.S. acknowledge financial support by Quebec Research Fund Nature and Technologies (FRQNT), Team Research Project (FRQNT-326563). A.H.A. and A.S. also acknowledge the support received from the TechAccelR program at McGill University. J.S. and K.J. acknowledge the financial support of FRQNT Postdoctoral Research Scholarships (333671, 329936).

Conflict of Interest

The authors declare no conflict of interest.

Data Availability Statement

The data that support the findings of this study are available from the corresponding author upon reasonable request.

Keywords

digital light processing, ferroelectric metamaterial, piezoelectricity and pyroelectricity, stretching and bending-dominated lattice, wearable device

Received: September 19, 2024
Revised: November 23, 2024
Published online:

[1] V. M. Shalaev, *Nat. Photonics* **2007**, *1*, 41.
[2] J. Li, C. T. Chan, *Phys. Rev. E* **2004**, *70*, 055602.
[3] a) K. Bertoldi, P. M. Reis, S. Willshaw, T. Mullin, *Adv. Mater.* **2010**, *22*, 361; b) H. Chen, J. Shi, A. Akbarzadeh, *Adv. Funct. Mater.* **2023**, *33*, 2306022.
[4] Y. Wang, L. Li, D. Hofmann, J. E. Andrade, C. Daraio, *Nature* **2021**, *596*, 238.
[5] a) A. Arnau, D. Soares, in *Piezoelectric Transducers and Applications*, (Ed: A. A. Vives), Springer, Berlin, Heidelberg **2008**, p. 1, https://doi.org/10.1007/978-3-540-77508-9_1; b) C. R. Bowen, J. Taylor, E. LeBoulbar, D. Zabek, A. Chauhan, R. Vaish, *Energy Environ. Sci.* **2014**, *7*, 3836.
[6] H. Cui, D. Yao, R. Hensleigh, H. Lu, A. Calderon, Z. Xu, S. Davaria, Z. Wang, P. Mercier, P. Tarazaga, X. Zheng, *Science* **2022**, *376*, 1287.
[7] H. Lu, H. Cui, G. Lu, L. Jiang, R. Hensleigh, Y. Zeng, A. Rayes, M. K. Panduranga, M. Acharya, Z. Wang, A. Irimia, F. Wu, G. P. Carman, J. M. Morales, S. Putterman, L. W. Martin, Q. Zhou, X. Zheng, *Nat. Commun.* **2023**, *14*, 2418.
[8] S. Chen, P. Zhu, L. Mao, W. Wu, H. Lin, D. Xu, X. Lu, J. Shi, *Adv. Mater.* **2023**, *35*, 2208256.
[9] a) S. Wada, K. Takeda, T. Muraishi, H. Kakemoto, T. Tsurumi, T. Kimura, *Jpn. J. Appl. Phys.* **2007**, *46*, 7039; b) X. Ding, B. Shen, J. Zhai, Z. Xu, F. Fu, J. Zhang, X. Yao, *Ferroelectrics* **2010**, *401*, 30.

[10] Y. Huan, X. Wang, J. Fang, L. Li, *J. Eur. Ceram. Soc.* **2014**, *34*, 1445.
[11] Z.-Y. Shen, J.-F. Li, *J. Ceram. Soc. Jpn.* **2010**, *118*, 940.
[12] a) M. Yan, Z. Xiao, J. Ye, X. Yuan, Z. Li, C. Bowen, Y. Zhang, D. Zhang, *Energy Environ. Sci.* **2021**, *14*, 6158; b) C. R. Bowen, A. Perry, A. C. F. Lewis, H. Kara, *J. Eur. Ceram. Soc.* **2004**, *24*, 541; c) M. Yan, J. Zhong, S. Liu, Z. Xiao, X. Yuan, D. Zhai, K. Zhou, Z. Li, D. Zhang, C. Bowen, Y. Zhang, *Nano Energy* **2021**, *88*, 106278; d) Q. Xu, Z. Wang, J. Zhong, M. Yan, S. Zhao, J. Gong, K. Feng, J. Zhang, K. Zhou, J. Xie, H. Xie, D. Zhang, Y. Zhang, C. Bowen, *Adv. Funct. Mater.* **2023**, *33*, 2304402; e) Y. Zhang, M. Xie, J. Roscow, Y. Bao, K. Zhou, D. Zhang, C. R. Bowen, *J. Mater. Chem. A* **2017**, *5*, 6569.
[13] A. Yang, C.-A. Wang, R. Guo, Y. Huang, *J. Am. Ceram. Soc.* **2010**, *93*, 1984.
[14] G. Zhang, P. Zhao, X. Zhang, K. Han, T. Zhao, Y. Zhang, C. K. Jeong, S. Jiang, S. Zhang, Q. Wang, *Energy Environ. Sci.* **2018**, *11*, 2046.
[15] M. Xie, Y. Zhang, M. J. Kraśny, C. Bowen, H. Khanbareh, N. Gathercole, *Energy Environ. Sci.* **2018**, *11*, 2919.
[16] a) X. Zheng, H. Lee, T. H. Weisgraber, M. Shusteff, J. DeOtte, E. B. Duoss, J. D. Kuntz, M. M. Biener, Q. Ge, J. A. Jackson, S. O. Kucheyev, N. X. Fang, C. M. Spadaccini, *Science* **2014**, *344*, 1373; b) J. Bauer, L. R. Meza, T. A. Schaedler, R. Schwaiger, X. Zheng, L. Valdevit, *Adv. Mater.* **2017**, *29*, 1701850.
[17] J. B. Berger, H. N. G. Wadley, R. M. McMeeking, *Nature* **2017**, *543*, 533.
[18] J. Shi, H. Mofatteh, A. Mirabolghasemi, G. Desharnais, A. Akbarzadeh, *Adv. Mater.* **2021**, *33*, 2102423.
[19] a) L. R. Meza, A. J. Zelhofer, N. Clarke, A. J. Mateos, D. M. Kochmann, J. R. Greer, *Proc. Natl. Acad. Sci. USA* **2015**, *112*, 11502; b) X. Zheng, W. Smith, J. Jackson, B. Moran, H. Cui, D. Chen, J. Ye, N. Fang, N. Rodriguez, T. Weisgraber, C. M. Spadaccini, *Nat. Mater.* **2016**, *15*, 1100.
[20] M. F. Ashby, *Philos. Trans. R. Soc., A* **2005**, *364*, 15.
[21] V. S. Deshpande, M. F. Ashby, N. A. Fleck, *Acta Mater.* **2001**, *49*, 1035.
[22] H. Cui, R. Hensleigh, D. Yao, D. Maurya, P. Kumar, M. G. Kang, S. Priya, X. Zheng, *Nat. Mater.* **2019**, *18*, 234.
[23] a) Z. Jiang, Y. Sun, J. Chen, Y. Zeng, *J. Adv. Ceram.* **2024**, *13*, 987; b) J. Ye, H. Gong, Y. Zhang, Q. Xu, X. Zhou, M. Yan, D. Zhai, K. Zhou, D. Zhang, C. Bowen, *Addit. Manuf.* **2024**, *79*, 103915; c) Y. Hong, S. Liu, X. Yang, W. Hong, Y. Shan, B. Wang, Z. Zhang, X. Yan, W. Lin, X. Li, Z. Peng, X. Xu, Z. Yang, *Nat. Commun.* **2024**, *15*, 5030.
[24] J. Shi, K. Ju, H. Chen, A. Mirabolghasemi, S. Akhtar, A. Sasmito, A. Akbarzadeh, *Nano Energy* **2024**, *123*, 109385.
[25] a) Y. Zeng, L. Jiang, Y. Sun, Y. Yang, Y. Quan, S. Wei, G. Lu, R. Li, J. Rong, Y. Chen, Q. Zhou, *Micromachines* **2020**, *11*; b) S. M. Gaytan, M. A. Cadena, H. Karim, D. Delfin, Y. Lin, D. Espalin, E. MacDonald, R. B. Wicker, *Ceram. Int.* **2015**, *41*, 6610; c) Z. Chen, X. Song, L. Lei, X. Chen, C. Fei, C. T. Chiu, X. Qian, T. Ma, Y. Yang, K. Shung, Y. Chen, Q. Zhou, *Nano Energy* **2016**, *27*, 78; d) W. Wang, J. Sun, B. Guo, X. Chen, K. P. Ananth, J. Bai, *J. Eur. Ceram. Soc.* **2020**, *40*, 682; e) J. Cheng, Y. Chen, J.-W. Wu, X.-R. Ji, S.-H. Wu, *Sensors* **2019**, *19*, 4078; f) Z. Jiang, L. Cheng, Y. Zeng, Z. Zhang, Y. Zhao, P. Dong, J. Chen, *Ceram. Int.* **2022**, *48*, 6477.
[26] a) Y. Zhang, J. Roscow, R. Lewis, H. Khanbareh, V. Y. Topolov, M. Xie, C. R. Bowen, *Acta Mater.* **2018**, *154*, 100; b) G. Martínez-Ayuso, M. I. Friswell, H. Haddad Khodaparast, J. I. Roscow, C. R. Bowen, *Acta Mater.* **2019**, *173*, 332.
[27] L. R. Meza, S. Das, J. R. Greer, *Science* **2014**, *345*, 1322.
[28] a) B. Jaffe, W. Cook, *Academic London* **1971**, *21*, 237; b) H. Takahashi, Y. Numamoto, J. Tani, S. Tsurekawa, *Jpn. J. Appl. Phys.* **2006**, *45*, 7405; c) H. Takahashi, Y. Numamoto, J. Tani, S. Tsurekawa, *Jpn. J. Appl. Phys.* **2008**, *47*, 8468; d) Y. q. Tan, J. l. Zhang, Z. Zhang, C. l. Wang, presented at 2011 Symposium on Piezoelectricity, Acoustic Waves and Device Applications (SPAWDA) December **2011**, 589; e) T. Karaki, K. Yan, M. Adachi, *Jpn. J. Appl. Phys.* **2007**, *46*, 7035; f) N. Ma, B.-P. Zhang, W.-G. Yang, D. Guo, *J. Eur. Ceram. Soc.* **2012**, *32*, 1059.
[29] K. A. Klicker, J. V. Biggers, R. E. Newnham, *J. Am. Ceram. Soc.* **1981**, *64*, 5.
[30] a) H. I. Schlaberg, J. S. Duffy, *Sens. Actuators, A* **1994**, *44*, 111; b) C. Park, Z. Ounaies, K. E. Wise, J. S. Harrison, *Polymer* **2004**, *45*, 5417; c) Q. Sun, W. Xia, Y. Liu, P. Ren, X. Tian, T. Hu, *IEEE Transactions on Ultrasonics, Ferroelectrics, and Frequency Control* **2020**, *67*, 975; d) Y. Huang, G. Rui, Q. Li, E. Allahyarov, R. Li, M. Fukuto, G.-J. Zhong, J.-Z. Xu, Z.-M. Li, P. L. Taylor, L. Zhu, *Nat. Commun.* **2021**, *12*, 675.
[31] a) X.-G. Chen, Y.-Y. Tang, H.-P. Lv, X.-J. Song, H. Peng, H. Yu, W.-Q. Liao, Y.-M. You, R.-G. Xiong, *J. Am. Chem. Soc.* **2023**, *145*, 1936; b) Y. Hu, K. Parida, H. Zhang, X. Wang, Y. Li, X. Zhou, S. A. Morris, W. H. Liew, H. Wang, T. Li, F. Jiang, M. Yang, M. Alexe, Z. Du, C. L. Gan, K. Yao, B. Xu, P. S. Lee, H. J. Fan, *Nat. Commun.* **2022**, *13*, 5607; c) B. Wang, J. Hong, Y. Yang, H. Zhao, L. Long, L. Zheng, *Matter* **2022**, *5*, 1296.
[32] A. Graves, S. Fernández, J. Schmidhuber, presented at Artificial Neural Networks: Formal Models and Their Applications – ICANN 2005, Springer, Berlin, Heidelberg **2005**.